

Dependent Scattering in Thick and Concentrated Colloidal Suspensions

Refet Ali Yalcin, Thomas Lee, Ghereh Natalie Kashanchi, Johannes Markkanen, Ricardo Martinez, Sarah H. Tolbert, and Laurent Pilon*



Cite This: *ACS Photonics* 2022, 9, 3318–3332



Read Online

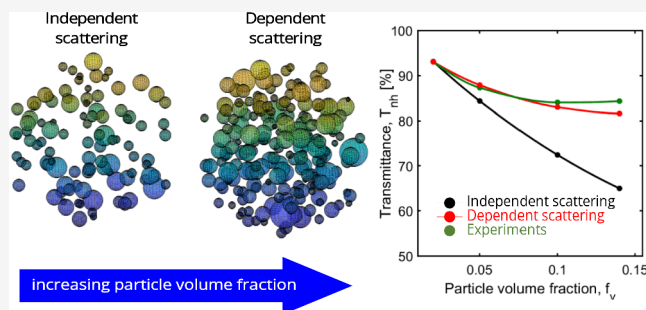
ACCESS |

 Metrics & More

 Article Recommendations

ABSTRACT: This study demonstrates numerically and experimentally that dependent scattering occurs in colloidal suspensions and can, counterintuitively, cause their transmittance to increase with increasing particle volume fraction. Radiation transfer through colloidal suspensions has been modeled with the radiative transfer equation (RTE) assuming independent scattering. Then, the effective absorption and scattering coefficients of the disperse medium are predicted as the sum of the cross sections of all particles divided by the volume of suspension. However, this approach is not valid when the average interparticle distance is on the same order of magnitude as the wavelength, corresponding to large particle concentrations. The latter situation is referred to as dependent scattering. Rigorously accounting for dependent scattering requires solving Maxwell's equations, but is limited to relatively thin suspensions. Here, we extend the Radiative Transfer with Reciprocal Transactions (R^2T^2) method to predict the normal-hemispherical transmittance of thick and concentrated plane-parallel slabs of nonabsorbing nanoparticle suspensions and to rigorously account for dependent scattering effects. The radiation characteristics of a large number of particle ensembles were estimated using the superposition T-matrix method and the RTE was solved using Monte Carlo method combined with strategies for sampling the previously computed radiation characteristics. A wide range of particle size parameter, volume fraction, and optical properties as well as colloidal suspension thickness were investigated. Dependent scattering effects were found to prevail for particle volume fractions as low as 1% depending on the particle size and refractive index. Evidences of dependent scattering were also observed experimentally in the visible normal-hemispherical transmittance of 10 mm thick colloidal suspensions of silica nanoparticles with diameter between 16 and 30 nm and particle volume fraction ranging from 2% to 15%. Moreover, good agreement was found between experimental measurements and numerical predictions from the R^2T^2 method. By contrast, assuming independent scattering underestimated systematically the normal-hemispherical transmittance, especially for large particle volume fraction. As such, this paper presents, for the first time, experimental validation of the R^2T^2 method and its ability to account for dependent scattering.

KEYWORDS: incoherent scattering, nanofluids, solar thermal energy conversion, aerosols, paints



1. INTRODUCTION

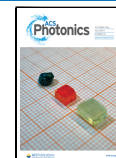
Colloidal suspensions consist of randomly distributed nanoparticles kept suspended in a fluid (liquid or gas) thanks to interparticle repulsion and Brownian motion. They have found a wide range of applications including white,¹ colored,² and solar absorbing paints.³ They have also been called nanofluids and found applications in solar thermal energy conversion.^{4–8} They also occur naturally in atmospheric aerosols,⁹ clouds,¹⁰ fogs,¹¹ snow, and planetary regoliths.¹² In addition, nanoemulsions are metastable dispersions of two immiscible fluids in which the dispersed phase droplets have a mean radius of less than 100 nm.¹³ They are being considered for drug delivery as well as for food and personal care products.^{14–16}

Understanding light scattering through nanoemulsions can enable their careful optical characterization.¹⁶

Radiation transfer through scattering and absorbing colloidal suspensions has often been simulated by solving the radiative transfer equation (RTE) to predict the local radiation intensity field.^{6–8} To do so, the absorption and scattering coefficients of the suspensions were predicted as the sum of the contributions

Received: May 3, 2022

Published: October 4, 2022



from all constitutive particles.¹⁷ This approach is based on the so-called “independent scattering” approximation and holds when the particles are sufficiently dilute and distant from one another.¹⁸ If the particles are spherical, the Lorenz-Mie theory can be used to predict the absorption and scattering cross sections of individual particles and their scattering phase function.¹⁷ Independent scattering prevails if (i) the suspension is dilute so that particles are separated by a distance larger than several wavelengths depending on their size,¹⁸ (ii) the observation point resides sufficiently far from any particle; (iii) the number of particles in the suspension is very large; (iv) all particles move randomly and independently of each other in the medium; (v) the physical state of each particle is independent of its position and of the states and positions of all the other particles; and (vi) the particle ensemble is fully ergodic, that is, its average characteristics can be deducted from sufficiently large samples randomly collected from the system.¹⁹ For example, Mishchenko et al.²⁰ observed experimentally that the independent scattering assumption was valid for randomly dispersed spherical latex particles, 700 nm in diameter and suspended in water for particle volume fraction smaller than 2% at wavelengths 595 and 696 nm. Beyond this critical volume fraction, the so-called “dependent” scattering prevailed.^{20–22} Here, the dependent scattering effects encompassed structural correlations, near field effects, as well as multiple scattering.

Alternatively, the absorptivity, reflectivity, and transmissivity of photonic structures can be calculated by direct solution of Maxwell’s equations when the structure size is of the same order of magnitude as the wavelength of the incident electromagnetic wave. However, this approach is impractical for colloidal suspensions with thickness much larger than the wavelength of interest, that is, in the micrometer to centimeter range or even larger (e.g., clouds or fog). A direct solution of Maxwell’s equations for such large systems cannot be obtained with current computing capabilities due to limitations in the available random-access memory (RAM), even with state-of-the-art scientific computing clusters.

More recently, Muinonen et al.²³ and Väisänen et al.²⁴ developed an algorithm based on the Radiative Transfer with Reciprocal Transactions (R^2T^2) method that solves the RTE with the ability to account for dependent scattering. First, the authors predicted the radiation characteristics of hundreds of spherical particle ensembles consisting of a large number ($\sim 100\text{--}1000$) of absorbing spherical particles by solving Maxwell’s equations. Each particle ensemble was extracted from the center of a much larger cube populated with randomly distributed monodisperse spheres with the desired particle volume fraction. Second, the absorption and scattering cross sections and the T-matrices of the particle ensembles were computed using the Fast Superposition T-matrix method (FaSTMM).²⁵ Finally, the RTE was solved using the Monte Carlo method within the medium among randomly sampled particle ensembles whose radiation characteristics were previously calculated. The authors demonstrated that their method was capable of estimating the radiation intensity field in a spherical domain of colloidal suspensions consisting of monodisperse particles of radius r_s , in air, by comparing the predictions from the R^2T^2 method with those obtained from direct solution of Maxwell’s equations. Specifically,²⁴ the particle volume fraction was $f_v = 0.25$, with the particle size parameter $x_s = 2\pi r_s/\lambda = 2$, while the suspension diameter D was much larger than the wavelength λ , such that $2\pi D/\lambda =$

100. The R^2T^2 method has also been extended to nonspherical particles.²⁰

The present study aims to develop a computational framework capable of simulating radiation transfer in a plane-parallel slab of absorbing and scattering media consisting of dispersed spherical particles with large volume fraction and arbitrary thickness so as to gain insight into dependent scattering phenomena in colloidal suspensions. The study specifically aims to identify the conditions under which dependent scattering must be accounted for in thick and concentrated colloidal suspensions. It is limited to non-absorbing particles when diffraction, interferences, dependent and multiple scattering dominate and are unimpeded by absorption.²⁶ Special attention was paid to the effects of (i) particle size distribution, (ii) volume fraction, and (iii) refractive indices. Predictions from the numerical simulation tools were also compared with experimental measurements of the normal-hemispherical spectral transmittance of aqueous colloidal suspensions of polydisperse silica nanoparticles with radius between 5 and 15 nm and volume fraction ranging from 2% to 15%. This study considers a relatively simple system in order to be able to faithfully simulate and characterize the experimental samples. In addition, silica nanoparticle suspensions were chosen because they are nonabsorbing in the visible when dependent scattering is not hindered by absorption, as previously discussed.

2. BACKGROUND

2.1. Electromagnetic Waves through Suspensions of Particles and Aggregates.

Electromagnetic wave transport in heterogeneous structures, such as particle suspensions and aggregates, are governed by Maxwell’s equations. The solutions of these equations can be obtained by various methods, including the finite difference time domain (FDTD),²⁷ the discrete dipole approximation (DDA),²⁸ the finite element (FEM),²⁹ and the superposition T-matrix³⁰ methods. However, these methods of solution are computationally intensive and can be used only for particle systems with a size on the same order of magnitude as the incident wavelength.³¹ Comparatively, the superposition T-matrix method is computationally less intensive than the other methods that are based on discretizing the computational domain into small elements, meshes, or dipoles.³² In fact, the superposition T-matrix method can solve Maxwell’s equations for an ensemble of spheres based on superposition principles and on analytical solutions of Maxwell’s equations such as the Lorenz-Mie theory.³³ Conveniently, the superposition T-matrix method has been implemented for GPU computing,³⁴ making it possible to account for a large number of spheres without requiring excessively long computational time. Unfortunately, as previously mentioned, it still cannot be used for solving Maxwell’s equations in millimeter-thick colloidal suspensions.

2.2. Radiation Transfer Theory. 2.2.1. Radiative Transfer Equation.

Instead of solving Maxwell’s equations, one can predict the local radiation intensity field $I_\lambda(\mathbf{r}, \Omega)$ at location \mathbf{r} in solid angle Ω by solving the RTE expressing energy conservation principles for the local spectral radiation intensity I_λ within the medium.¹⁷ In a nonemitting (i.e., cold), absorbing, and scattering colloidal suspension, the RTE is expressed as¹⁷

$$\frac{dI_\lambda(\mathbf{r}, \Omega)}{ds} = -\kappa_\lambda I_\lambda(\mathbf{r}, \Omega) - \sigma_{s,\lambda} I_\lambda(\mathbf{r}, \Omega) + \frac{\sigma_{s,\lambda}}{4\pi} \int_{4\pi} I_\lambda(\mathbf{r}, \Omega') \Phi_{T,\lambda}(\Omega', \Omega) d\Omega' \quad (1)$$

where κ_λ and $\sigma_{s,\lambda}$ are the effective absorption and scattering coefficients of the suspension and $\Phi_{T,\lambda}(\Omega', \Omega)$ is its scattering phase function. The RTE given in eq 1 accounts for attenuation of the intensity due to absorption and out-scattering as well as its enhancement from in-scattering and multiple scattering along a given direction of propagation. Solving the RTE consists of two consecutive steps: (1) predicting the effective radiation characteristics κ_λ , $\sigma_{s,\lambda}$, and $\Phi_{T,\lambda}(\Omega', \Omega)$ of the heterogeneous medium at wavelength λ and (2) solving the RTE to predict the local radiation intensity $I_\lambda(\mathbf{r}, \Omega)$ in different directions. The predicted intensity emerging from the boundaries of the computational domain encompassing the suspension can be used to predict the spectral normal–normal or normal–hemispherical reflectances and transmittances of the suspension of any arbitrary geometry. For example, the normal–hemispherical transmittance of a plane-parallel slab of thickness L can be expressed as¹⁷

$$T_{nh} = \frac{\int_0^{2\pi} \int_0^{\pi/2} I_{\lambda,t}(L, \theta_t, \varphi_t) \cos \theta_t \sin \theta_t d\theta_t d\varphi_t}{I_{\lambda,i} \Delta \Omega_i} \quad (2)$$

where θ_t and φ_t are the polar and azimuthal angles of the transmitted intensity $I_{\lambda,t}(L, \theta_t, \varphi_t)$ defined with respect to the outward normal to the back surface of the suspension, while $I_{\lambda,i}$ is the intensity normally incident onto the slab in solid angle $\Delta \Omega_i$.

2.2.2. Independent Scattering. As previously discussed, independent scattering assumes that the effective absorption and scattering coefficients of the suspension can be computed as the sum of the absorption and scattering cross sections of the different particles, based on superposition principles. For example, the radiation characteristics $\kappa_\lambda^{\text{ind}}$, $\sigma_{s,\lambda}^{\text{ind}}$, and $\Phi_{T,\lambda}^{\text{ind}}(\Omega', \Omega)$ of a suspension consisting of monodisperse spherical particles of radius r_s and complex index of refraction $m_s = n_s + ik_s$ in a nonabsorbing medium of refractive index n_m can be expressed as¹⁷

$$\sigma_{s,\lambda}^{\text{ind}} = N_T \pi r_s^2 Q_{\text{sca},\lambda}^M(x_s, m) \quad \text{and} \quad \kappa_\lambda^{\text{ind}} = N_T \pi r_s^2 Q_{\text{abs},\lambda}^M(x_s, m) \quad (3)$$

$$\Phi_{T,\lambda}^{\text{ind}}(\Omega', \Omega) = \Phi_\lambda^M(\Omega', \Omega) \quad (4)$$

where $N_T = 3f_v/4\pi r_s^3$ is the number of particles per unit volume, while f_v is the particle volume fraction in the suspension. Here, the absorption $Q_{\text{abs},\lambda}^M(x_s, m)$ and scattering $Q_{\text{sca},\lambda}^M(x_s, m)$ efficiency factors and the scattering phase function $\Phi_\lambda^M(\Omega', \Omega)$ of a single spherical particle can be predicted by the Lorenz-Mie theory and depend on the particle size parameter $x_s = 2\pi r_s/\lambda$ and the relative complex index of refraction $m = m_s/n_m$.³³

2.2.3. Dependent Scattering. As the particle concentration in the suspension increases, dependent scattering may prevail depending on the particle size parameter x_s and some measure of the particle proximity.¹⁸ Tien and Drolen³⁵ reviewed the different analytical models developed prior to 1987 to account for dependent scattering in packed beds and fluidized beds.^{36–39} Dependent scattering was accounted for by expressing the average scattering efficiency factor Q_{sca}^D of a

single particle in the form $Q_{\text{sca}}^D(x_s, m, f_v, c/\lambda) = F(f_v, c/\lambda) Q_{\text{sca}}^M(x_s, m)$, where $F(f_v, c/\lambda)$ is a form factor depending on the volume fraction f_v and the ratio c/λ of the clearing distance c between adjacent particles and the wavelength λ . The analyses typically considered simple arrangements of equidistant and monodisperse spheres in an ordered structure. Tien and Drolen³⁵ also proposed a scattering map indicating the areas where dependent and independent scattering prevail in the volume fraction f_v versus particle size parameter x_s diagram. The independent scattering assumption prevails if the volume fraction is such that $f_v < 0.6\%$ or, for $f_v > 0.6\%$, if the clearing distance to wavelength ratios are such that $c/\lambda > 0.5$ corresponding to

$$f_v > \left(\frac{0.9047}{1 + \pi/(2x_s)} \right)^3 \quad (5)$$

assuming a rhombohedral packing of particles. Note also that the effects of dependent scattering on the scattering phase function or on the asymmetry factor were not considered by Tien and co-workers. The reader is referred to our recent study for a detailed review of the literature focused on dependent scattering in the scattering cross sections and asymmetry factors of bispheres and random or ordered particle suspensions.

Recently, we demonstrated that the scattering efficiency factor and asymmetry factor should be written respectively as $Q_{\text{sca}}^D(x_s, m, \bar{d}/\lambda)$ and $g^D(x_s, m, \bar{d}/\lambda)$, where \bar{d} is the average interparticle distance without resorting to the form factor $F(f_v, c/\lambda)$ or considering f_v and c or a specific particle arrangement.⁴⁰ In addition, an alternative regime map was proposed to identify the dependent vs independent scattering regimes in terms of x_s versus \bar{d}/λ so as to reflect these new developments.⁴⁰ Moreover, different transition criteria from dependent to independent scattering regimes were obtained for Q_{sca}^D and g^D of ensembles of nonabsorbing particles.¹⁸

Alternatively, Mishchenko¹² successfully used the static structure factor to account for dependent scattering in the asymmetry factor and scattering phase function of densely packed particles representative of planetary regoliths and soil particles. The same “phenomenological patch” was used to match predictions of the vector RTE with experimental measurements of the Stokes reflection matrix of densely packed suspension of latex particles 700 nm in diameter with volume fraction f_v equal to 2%, 5%, and 10%.²⁰

Finally, the Foldy-Lax equations are mathematically equivalent to Maxwell's equations and presented in the form of a Neumann series solutions.⁴¹ In their recent study, Fuji et al.⁴² examined the integral radiation characteristics of polydisperse colloidal suspensions with different particle volume fractions. The authors reported the asymmetry factor and the scattering coefficient of fat emulsions by considering the first-order term of the Foldy-Lax equations for droplet diameter ranging from 20 to 690 nm with an average of 214 nm for volume fraction between 0.1% and 20%. They also observed dependent scattering effects in the scattering coefficient and asymmetry factor for different volume fractions.

2.3. Dense Medium Radiative Transfer (DMRT). Among methods accounting for dependent scattering effects, the T-matrix is the most accurate since it accounts for all the relevant phenomena including specular boundary reflection and near field effects. However, it is also the most computationally intensive method, making it impractical for

simulating radiation transfer through thick and dense suspensions. As an alternative, Tsang and Ishimaru⁴³ derived what they called the “dense medium radiative transfer (DMRT)” equations governing the Stoke vector from the second moment equations of the electromagnetic wave theory. To derive the DMRT equation, the authors first separated the scattered electric field into its coherent and incoherent components. The coherent field satisfies the Dyson equation⁴⁴ and can be approximated by an effective medium resulting in the boundary reflection and refraction. The incoherent component, which represents volumetric scattering by the heterogeneous medium, satisfies the Bethe–Salpeter equation. The correlated ladder approximation was used to simplify the Bethe–Salpeter equation⁴⁴ in which the Percus–Yevick approximation was invoked to account for the correlated locations of the scatterers.²⁴ Overall, the DMRT method solves the RTE using the scattering and extinction coefficients and the asymmetry factor calculated for dense medium using the ensemble averaged Mueller matrix based on the far field approximation. Thus, it does not account for near field effects or higher order multiple scattering.¹² As a result, dependent scattering in optically hard materials, such as metals and high refractive index particles in low refractive index media, cannot be accounted for accurately.

2.4. Radiative Transfer with Reciprocal Transactions (R^2T^2) Method. More recently, Muinonen et al.²³ and Väistönen et al.²⁴ developed the so-called Radiative Transfer with Reciprocal Transactions (R^2T^2) method based on the Monte Carlo method. The R^2T^2 method consists of three consecutive steps. **Step 1:** N particle ensembles, consisting of randomly distributed particles, are generated using a sufficiently large number of particles to ensure that the simulated domain is ergodic. **Step 2:** The incoherent T-matrices of the N particle ensembles are computed to eventually obtain the particle ensembles’ incoherent radiation characteristics $\beta_{\lambda,i}^{ic}$ and $\omega_{\lambda,i}^{ic}$. Here, to calculate the coherent and incoherent scattered electric field components, N particle ensembles with monodisperse particles were considered.⁴⁵ These ensembles should be large enough to represent the optical properties of an ergodic medium. Then, the coherent electric field $E^{sca,c}$ can be found by averaging over the electric fields E_i^{sca} scattered by all particle ensembles i ($1 \leq i \leq N$) according to²⁴

$$E^{sca,c} = \lim_{N \rightarrow \infty} \frac{1}{N} \sum_{i=1}^N E_i^{sca} \quad (6)$$

The total scattered electric field E_i^{sca} can be represented as²⁴

$$E_i^{sca} = \sum_{v=1}^{N_o} \sum_{w=-v}^v (a_{vw1} M_{vw} + a_{vw2} N_{vw}) \quad (7)$$

where M_{vw} and N_{vw} are the base vectors composed of vector spherical wave functions while $a_{vw1,i}$ and $a_{vw2,i}$ are the spherical vector wave function coefficients associated with each polarization. Then, it is possible to find the so-called T-matrix⁴⁶

$$\begin{pmatrix} a_{vw1,i} \\ a_{vw2,i} \end{pmatrix} = T_i \begin{pmatrix} f_{vw1} \\ f_{vw2} \end{pmatrix} \quad (8)$$

where f_{vw1} and f_{vw2} are the coefficients of the incident field E^{inc} . The T-matrix T_i for the i^{th} particle ensemble can be expressed

as the sum of the coherent T-matrix T^c , identical for all particle ensembles, and the incoherent T-matrix T_i^{ic} such that $T_i = T_i^{ic} + T^c$. By analogy with the coherent scattered electric field, the coherent T-matrix is defined as²⁴

$$T^c = \lim_{N \rightarrow \infty} \frac{1}{N} \sum_{i=1}^N T_i \quad \text{and} \quad T_i^{ic} = T_i - T^c \quad (9)$$

In other words, the sum of all incoherent T-matrices averaged over all particle ensembles is zero, that is, $\sum_{i=1}^N T_i^{ic} = 0$. After obtaining the incoherent T-matrix T_i^{ic} for the i^{th} particle ensemble, the coefficients of the incoherent scattered electric field, $a_{vw1,i}^{ic}$ and $a_{vw2,i}^{ic}$ can be obtained from

$$\begin{pmatrix} a_{vw1,i}^{ic} \\ a_{vw2,i}^{ic} \end{pmatrix} = T_i^{ic} \begin{pmatrix} f_{vw1} \\ f_{vw2} \end{pmatrix} \quad (10)$$

The incoherent scattering cross sections of the i^{th} particle ensemble can then be expressed as²⁴

$$C_{sca,i}^{ic} = \frac{1}{q^2} \sum_{v=1}^{N_o} \sum_{w=-v}^v (|a_{vw1,i}^{ic}|^2 + |a_{vw2,i}^{ic}|^2) \quad (11)$$

where $q = 2\pi/\lambda$ is the angular wavenumber and the integer N_o is the degree of expansion needed to ensure convergence. Similarly, the total scattering and extinction cross sections of the i^{th} particle ensemble are given by²⁴

$$C_{sca,\lambda,i}^{ic} = \frac{1}{q^2} \sum_{v=1}^{N_o} \sum_{w=-v}^v (|a_{vw1,i}^{ic}|^2 + |a_{vw2,i}^{ic}|^2) \quad (12)$$

$$C_{ext,\lambda,i}^{ic} = \frac{1}{q^2} \sum_{v=1}^{N_o} \sum_{w=-v}^v \text{Re}(a_{vw1,i}^{ic} + a_{vw2,i}^{ic}) \quad (13)$$

Moreover, the effective spectral incoherent extinction coefficient $\beta_{\lambda,i}^{ic}$ and the incoherent scattering albedo $\omega_{\lambda,i}^{ic}$ of a particle ensemble of volume V_e can be calculated according to²⁴

$$\beta_{\lambda,i}^{ic} = \frac{C_{sca,\lambda,i}^{ic} + C_{abs,\lambda,i}}{V_e} \quad \text{and} \quad \omega_{\lambda,i}^{ic} = \frac{C_{sca,\lambda,i}^{ic}}{C_{sca,\lambda,i}^{ic} + C_{abs,\lambda,i}} \quad (14)$$

where the total absorption cross-section of the i^{th} particle ensemble is given by

$$C_{abs,\lambda,i} = C_{ext,\lambda,i} - C_{sca,\lambda,i} \quad (15)$$

Finally, the absorption and scattering coefficients of the i^{th} ensemble can be expressed as

$$\kappa_{\lambda,i} = \beta_{\lambda,i}^{ic} (1 - \omega_{\lambda,i}^{ic}) \quad \text{and} \quad \sigma_{s,\lambda,i}^{ic} = \beta_{\lambda,i}^{ic} \omega_{\lambda,i}^{ic} \quad (16)$$

Step 3: The Monte Carlo method traces rays for the spherical vector wave function coefficients in eq 10 and six different polarization states, including four linear polarizations (vertical, horizontal, $+45^\circ$, -45°) and two circular polarizations (right-handed and left-handed). Then, the Monte Carlo ray tracing method is used to solve the RTE using ensemble-averaged incoherent extinction coefficient, $\sum_{i=1}^N \beta_{\lambda,i}^{ic}/N$, and randomly sampled scattering albedo $\omega_{\lambda,i}^{ic}$ estimated in Step 2 as well as the polarization-dependent scattering phase functions which are generated at each scattering event using a randomly selected incoherent T-matrix and the local spherical vector wave function coefficients.²⁴

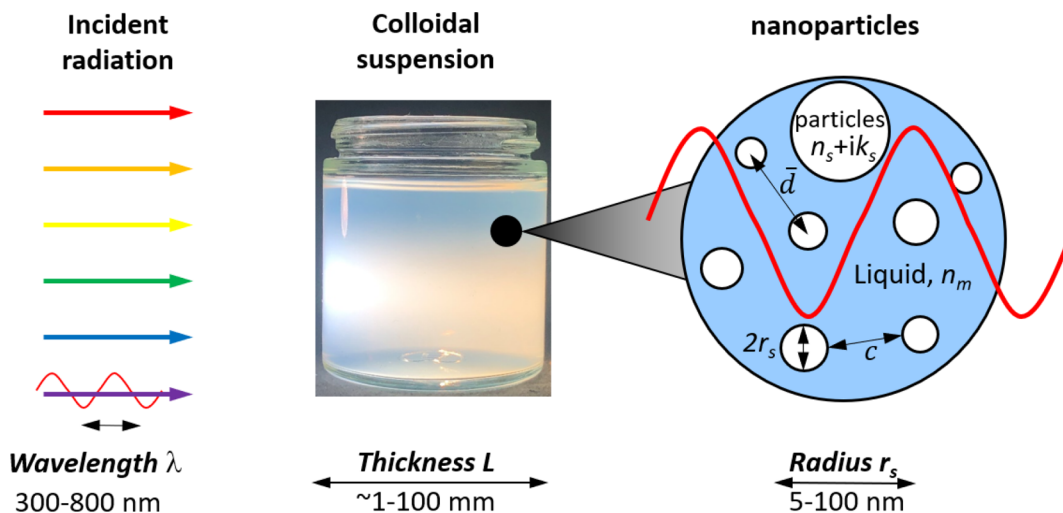


Figure 1. Illustration of light scattering in colloidal suspensions and the different length scales considered.

Three additional considerations arise when tracing rays through the medium considering particle ensembles. First, some particle ensembles may intersect with the boundaries of the suspension. Then, one can let the ensembles intersect or force them to remain within the confine of the plane parallel suspension. Second, the attenuation due to absorption and scattering can be computed from the boundary or from the center of the ensemble to the suspension surface. Third, two consecutive particle ensembles sampled in the Monte Carlo method between two consecutive scattering events may overlap, especially if the suspension is optically thick. Note that the T-matrices of all N ensembles were already computed before the ray tracing computation. Therefore, the overlap did not affect the T-matrix T_i (eq 8) used. All possible configurations were studied by Väistönen et al.²⁴ In brief, (i) letting the particle ensemble intersect with the boundaries of the suspension, (ii) accounting for attenuation from the origin of the ensemble, and (iii) allowing overlapping of consecutive particle ensembles led to better agreements with the solution of Maxwell's equations. The first two considerations are only important for suspension whose size is comparable to that of the particle ensembles. Overlapping of two consecutive ensembles is more likely optically thick, where the incoherent mean free path is smaller than the particle ensemble. This was not the case for the silica nanoparticles dispersed in water considered in the present study under visible light and featuring a small index mismatch and size parameter. However, in cases when large size parameters and/or high refractive index mismatch between particle and medium are considered, denying or allowing particle ensembles to overlap could have a significant impact on the predictions.

Finally, Penttilä et al.³¹ compared the results of the R^2T^2 method with those obtained by solving Maxwell's equations and found that the method can estimate the radiation intensity accurately in suspensions of particles in a spherical domain of air with dimensionless diameter $2\pi D/\lambda$ equal to 30.1, 64.8, 140, and 301, consisting of particles with $m_s = 1.5 + i10^{-4}$ and particle size parameter $x_s = 1.74$ and volume fraction $f_v = 20\%$. The authors also observed a large discrepancy between the predictions of the local intensity obtained from solving the RTE assuming independent scattering and from solving Maxwell's equations.

On the other hand, simulating thick media with the R^2T^2 method is relatively simple but it is more computationally intensive for large particle size parameters. However, this limitation is not crucial since dependent scattering effects are stronger for small particle size parameters. Moreover, the R^2T^2 method traces the electromagnetic waves from one spherical particle ensemble to the next in the heterogeneous medium. It uses the scattered radiation emerging from one particle ensemble as the incident wave onto the next particle ensemble. The R^2T^2 method calculates the scattering and absorption coefficients of the medium using the rigorous and accurate T-matrix method. However, the R^2T^2 method cannot account for the specular boundary reflection of the medium.²⁴ Note that specular boundary reflection of dense medium is not trivial to calculate from Fresnel equations since the effective refractive index of the suspension should be defined and the well-known effective medium approximations including the Maxwell–Garnett model are not appropriate for dense media and optically hard materials.⁴⁷

The objective of this study is to develop and validate a numerical framework capable of predicting the radiation intensity field in heterogeneous media of arbitrary thickness and accounting for dependent scattering and multiple scattering. It utilizes the R^2T^2 method to predict radiation transfer through colloidal suspensions consisting of randomly distributed nonabsorbing spherical particles. Particular attention was paid to the effect of particle size and volume fraction as well as suspension thickness. The solution of the RTE assuming independent scattering and using the effective radiation characteristics determined using the Lorenz-Mie theory was also considered since it has been widely used in the literature for simulating solar radiation transfer through nanofluids^{4–8} as well as to measure the particle size distribution using dynamic light scattering,^{48,49} for example. Experimental measurements of the normal-hemispherical transmittance in the visible part of the electromagnetic spectrum for aqueous colloidal suspensions of silica nanoparticles were also performed for particle volume fraction f_v up to 15%. The measurements were used to illustrate the occurrence of dependent scattering and to validate the different numerical methods used to simulate radiation transfer in colloidal suspensions.

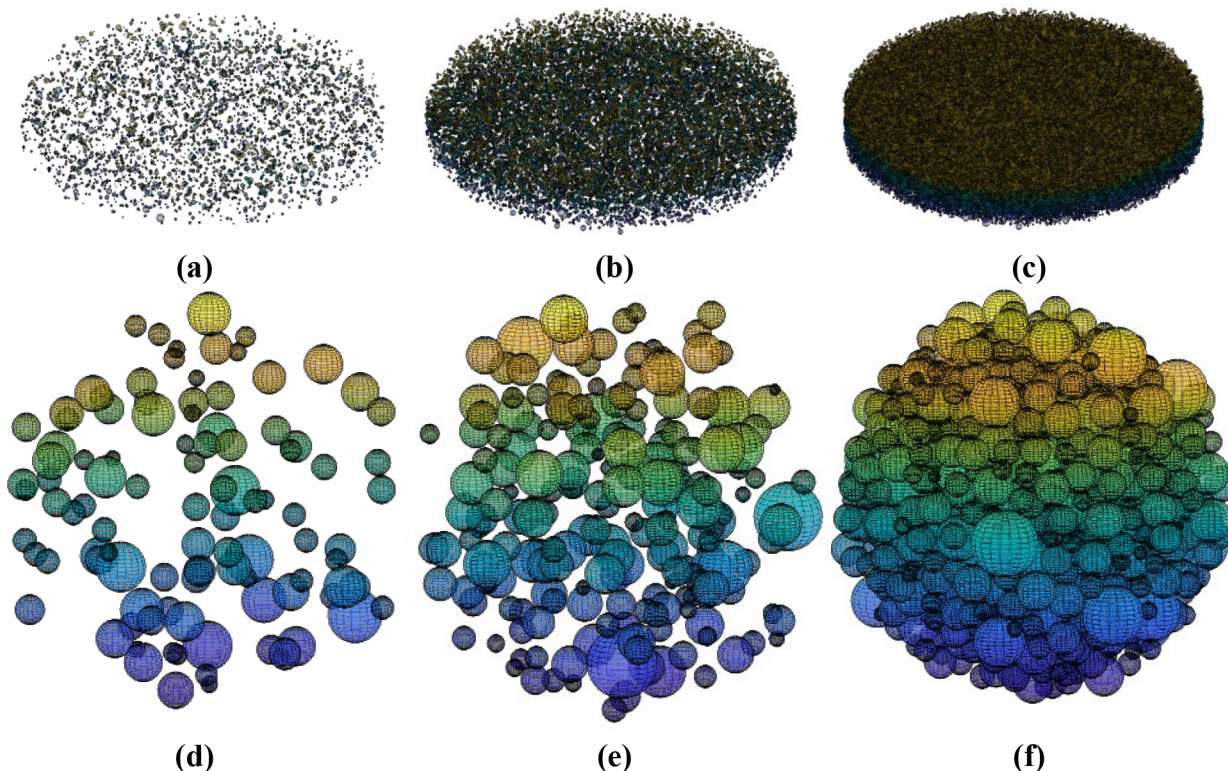


Figure 2. Cylindrical plane-parallel slabs $2 \mu\text{m}$ thick of randomly distributed monodisperse spherical particles of radius $r_s = 50 \text{ nm}$ simulated with the T-Matrix method for particle volume fraction (a) $f_v = 2\%$ (3766 spheres), (b) $f_v = 10\%$ (18625 spheres), and (c) $f_v = 35\%$ (74320 spheres). Example of particle ensembles of randomly distributed polydisperse spherical particles with log-normal size distribution such that $\bar{r}_s = 100 \text{ nm}$ and $\sigma = 20 \text{ nm}$ for particle volume fraction (d) $f_v = 5\%$, (e) $f_v = 10\%$, and (f) $f_v = 50\%$.

3. ANALYSIS

3.1. Problem Statement. Figure 1 illustrates the colloidal suspensions exposed to visible light investigated in the present study and the different length scales and parameters considered. The colloidal suspension was characterized by (i) the size distribution $f(r_s)$ of spherical particles of radius r_s , (ii) the particle volume fraction f_v , (iii) the particle spatial arrangement, (iv) the particle refractive index n_s ($k_s = 0$), (v) the continuous medium refractive index n_m at wavelength λ in the visible and near-infrared (400–900 nm), and (vi) the suspension thickness L .

3.2. Methods of Solution. For solving Maxwell's equations, the publicly available code CELES³⁴ implementing the superposition T-matrix method on GPU was used. A Gaussian beam of radius $1 \mu\text{m}$ was normally incident on a plane parallel slab of randomly distributed monodisperse or polydisperse particles. Due to the shape of the incident beam, we simulated a cylindrical particle suspension of thickness L and radius R_c . In fact, randomly dispersed particles were populated inside a large rectangular prism with dimensions $4R_c \times 4R_c \times 2L$. Then, a cylinder of thickness L and radius R_c was cropped from the center of the rectangular prism to eliminate any edge effects. The choice of R_c was important to ensure that the particle suspension could be treated as plane-parallel and that the number of photon bundles escaping the cylinder through the sides was negligible. These conditions were met for $R_c = 4L$, based on preliminary simulations. Figure 2 shows examples of simulated plane-parallel cylinders filled with monodisperse particles of radius $r_s = 50 \text{ nm}$ for volume fraction f_v equal to (a) 2%, (b) 10%, and (c) 35%. Simulations

based on GPU-based superposition T-Matrix method were performed on a Nvidia GeForce RTX 2080 Ti graphic card.

For thin film coatings, the cropped cylinder featured a relatively small radius R_c such that predictions of the transmittance by the T-matrix method could suffer from the effect of resonances such as those observed in photonic crystal structures.²⁴ To avoid this effect, 30 randomized particle slabs with the same dimensions were created and their normal-hemispherical transmittances were computed by the T-matrix method and averaged to yield the suspension normal-hemispherical transmittance. Simulations based on the R^2T^2 method were performed on Intel Xeon CPU E5-2650 v2 @ 2.60 GHz 16 core, 128 GB RAM workstation. The computing time varied from 0.1 to 52 h and increased with increasing particle size, volume fraction f_v , and suspension thickness L .

On the other hand, solution of the RTE assuming independent scattering were obtained using the Monte Carlo method. The effective radiation characteristics of the suspension were obtained thanks to the publicly available codes based on the Lorenz-Mie theory for monodisperse⁵⁰ and polydisperse⁵¹ spherical particles, as used in previous studies.⁵²

The code implementing the R^2T^2 method to account for dependent scattering effects described in ref.²⁴ was used after several modifications. First, the original particle ensemble generator was capable of creating ensembles consisting only of monodisperse randomly distributed particles.⁵³ Here, we modified the code to enable custom specification of the spatial and size distributions of the spherical particles. Second, the code could simulate radiation transfer through semi-infinite media with planar geometry.²⁴ Here, the code was modified to account for the finite thickness of plane-parallel slabs of

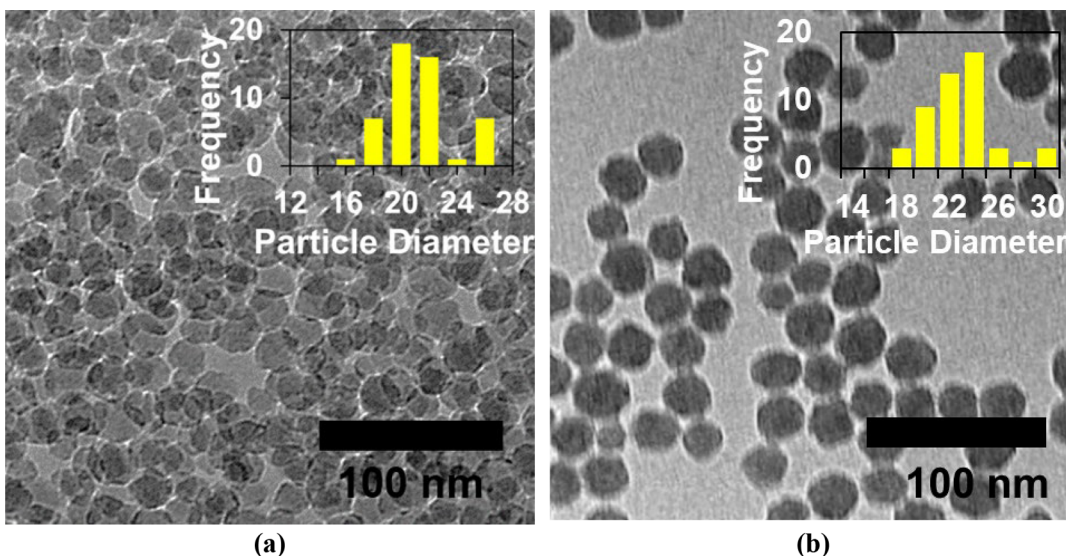


Figure 3. TEM images and particle diameter distributions of colloidal (a) Suspensions 1 and (b) 2.

particle suspensions to facilitate the comparison with experimental measurements. A total of $N = 500$ spherical particle ensembles of radius R_c were cropped from the center of N large cubes of height $4R_c$. Polydisperse particles were populated inside the cubes according to the desired particle size distribution $f(r_s)$ and particle volume fraction f_v . Figure 2d–f shows examples of particle ensembles cropped from the large cubes filled with polydisperse particles with log-normal size distribution with mean radius $\bar{r}_s = 100$ nm and standard deviation $\sigma = 20$ nm for volume fraction f_v equal to (d) 5%, (e) 10%, and (f) 50%.

4. MATERIALS AND METHODS

4.1. Sample Preparation, Materials, and Characterization. Two commercial aqueous silica colloidal suspensions were investigated experimentally, namely, Nyacol NexSil 12 (Suspension 1) and LUDOX TMA (Suspension 2) (see Figure 3). In both suspensions, the silica nanoparticles were negatively charged. Suspension 1 featured particles with diameter ranging from 16 to 28 nm stabilized with sodium counterions and initial concentration of 29–31 wt % at pH of 8.8–9.5. Suspension 2 was slightly acidic with low sodium level and silica particle diameter around 22 nm with concentration of 34 wt % for a density of 1.24 g/cm^3 . First, both suspensions were sonicated for 5 min at room temperature using an ultrasonicator (Fisher Scientific, Model 150E, 150 W) to fully disperse the individual silica particles that might have aggregated over time. Then, the sonicated solutions were diluted in deionized water to obtain four different particle volume fractions f_v ranging from 14 to 15 vol % (undiluted) to 2 vol %.

Transmission electron microscopy (TEM) images of nanoparticles from both suspensions were collected using a Tecnai G2 TF20 High-Resolution EM, CryoEM, and CryoET (FEI). To load the nanoparticles onto the TEM grids, an aliquot of the colloidal suspension was dried at 80°C and resuspended in ethanol prior to dipping the carbon coated grid into each suspension. An accelerating voltage of 200 kV and a TIETZ F415MP 16-megapixel $4\text{k} \times 4\text{k}$ CCD detector were used for imaging. Then, the silica nanoparticle size distribution was determined by measuring the diameter of 50 particles,

manually, using ImageJ. To determine the mass concentration of solids in the colloidal suspension, 0.5 mL of suspension were evaporated at 80°C in an oven. The mass was measured before and after evaporation and after calcination at 400°C for 6 h in an oxygen atmosphere to remove any organic phase. Then, the particle volume fraction was estimated from the silica particle mass fraction x (in wt %) in suspension provided by the manufacturer and based on the dilution ratio according to

$$f_v = \frac{V_s}{V_s + V_w} = \frac{\frac{x}{\rho_s}}{\frac{x}{\rho_s} + \frac{(1-x)}{\rho_w}} \quad (17)$$

where the densities⁵⁴ of bulk silica and water were taken as $\rho_s = 2.65 \text{ g/cm}^3$ and $\rho_w = 0.997 \text{ g/cm}^3$, respectively.

Table 1 summarizes the characterization results of the colloidal Suspensions 1 and 2. It indicates that there was no

Table 1. Concentration, Mean Particle Radius \bar{r}_s , Standard Deviation σ of Particle Size Distribution of Silica Nanoparticles in Colloids before and after Calcination

	wt % before calcination	wt % after calcination	mean particle radius \bar{r}_s (nm)	std dev σ (nm)	particle vol fraction f_v (%)
Suspension 1	32.6	32.3	10.1	1.2	2–14
Suspension 2	34.3	33.7	13.2	1.8	2–15

significant organic material in the suspension since the mass fraction of silica before and after calcination were very similar.

4.2. Transmittance Measurements. The normal-hemispherical transmittances of colloidal Suspensions 1 and 2 with different particle volume fractions were measured using a double-beam ultraviolet-visible (UV-vis) spectrophotometer (iS50, Thermo Scientific Fisher, U.S.A.) equipped with an integrating sphere (EVO220, Thermo Scientific Fisher, U.S.A.). Measurements were performed in the visible and near-infrared at wavelength λ ranging between 400 and 900 nm in 1 nm increments. A quartz cuvette with path length of 10 mm and containing the colloidal suspension was attached to the integrating sphere. The baseline measurement was performed with DI water in the cuvette for which the

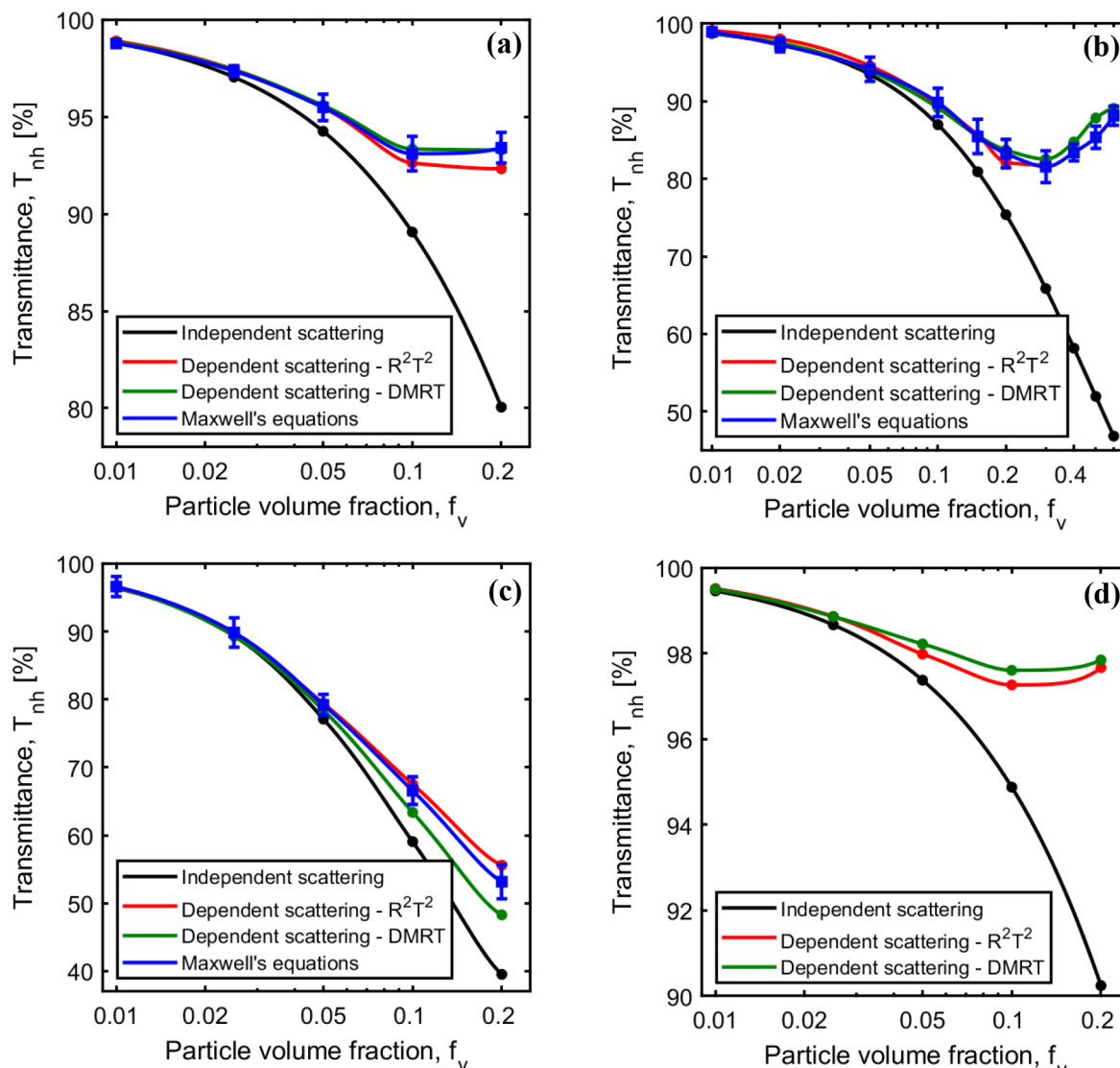


Figure 4. Comparison of the normal-hemispherical transmittance T_{nh} of particle suspensions of thickness L predicted numerically by the T-Matrix method (Maxwell's equations), the classical Monte Carlo method (independent scattering), DMRT method (dependent scattering - DMRT), and the R^2T^2 method (dependent scattering - R^2T^2) as a function of particle volume fraction for (a) monodisperse particles with $r_s = 50$ nm and $L = 5 \mu\text{m}$, (b) polydisperse particles with log-normal distribution with $\bar{r}_s = 50$ nm, $\sigma = 20$ nm, $L = 5 \mu\text{m}$, (c) monodisperse particles with $r_s = 150$ nm and $L = 5 \mu\text{m}$, and (d) monodisperse particles with $r_s = 5$ nm, $L = 2 \text{ mm}$. In all cases, $n = 1.5$ ($k = 0$) and $\lambda = 500$ nm.

normal-hemispherical transmittance was set to 100% so that the effects of boundary reflection and absorption by water could be corrected for.

5. RESULTS AND DISCUSSION

5.1. Comparison of the T-Matrix, Classical MC, DMRT, and R^2T^2 Methods. The normal-hemispherical transmittance T_{nh} of thin plane-parallel slabs of colloidal suspensions consisting of silica spherical nanoparticles was calculated in three different ways by solving (1) Maxwell's equations using the superposition T-matrix method, (2) the RTE based on the independent scattering approximation and using the classical Monte Carlo method, and (3) the RTE accounting for dependent scattering using the R^2T^2 method. The T-matrix method was used as a reference since it is the most rigorous method. Figure 4 compares the normal-hemispherical transmittance T_{nh} numerically predicted by the T-matrix, DMRT, and R^2T^2 methods for particle suspensions of thickness $L = 2$

μm or 2 mm as a function of particle volume fraction f_v for three different monodisperse particle suspensions with particle radius (a) $r_s = 50$ nm, (c) $r_s = 150$ nm, or (d) $r_s = 5$ nm along with (b) a polydisperse particle suspension with a log-normal size distribution of mean particle radius $\bar{r}_s = 50$ nm and standard deviation $\sigma = 20$ nm. In all cases, the silica particles were treated as nonabsorbing with relative refractive index $n = 1.5$ at wavelength $\lambda = 500$ nm. Note that the suspension thickness $L = 2 \mu\text{m}$ was arbitrarily selected to ensure that predictions by the T-matrix method could be obtained. However, the transmittance T_{nh} for a suspension of thickness $L = 2 \text{ mm}$ could not be computed by the T-matrix method even for a small particle radius (Figure 4d) due to limitations in the computing resources, as previously discussed. First, the DMRT method was able to capture the dependent scattering effects for small particles with radii $r_s = 5$ nm and $r_s = 50$ nm. Indeed, its predictions were in excellent agreement with those by the T-matrix method (Figure 4a,b,d), as well as those by the

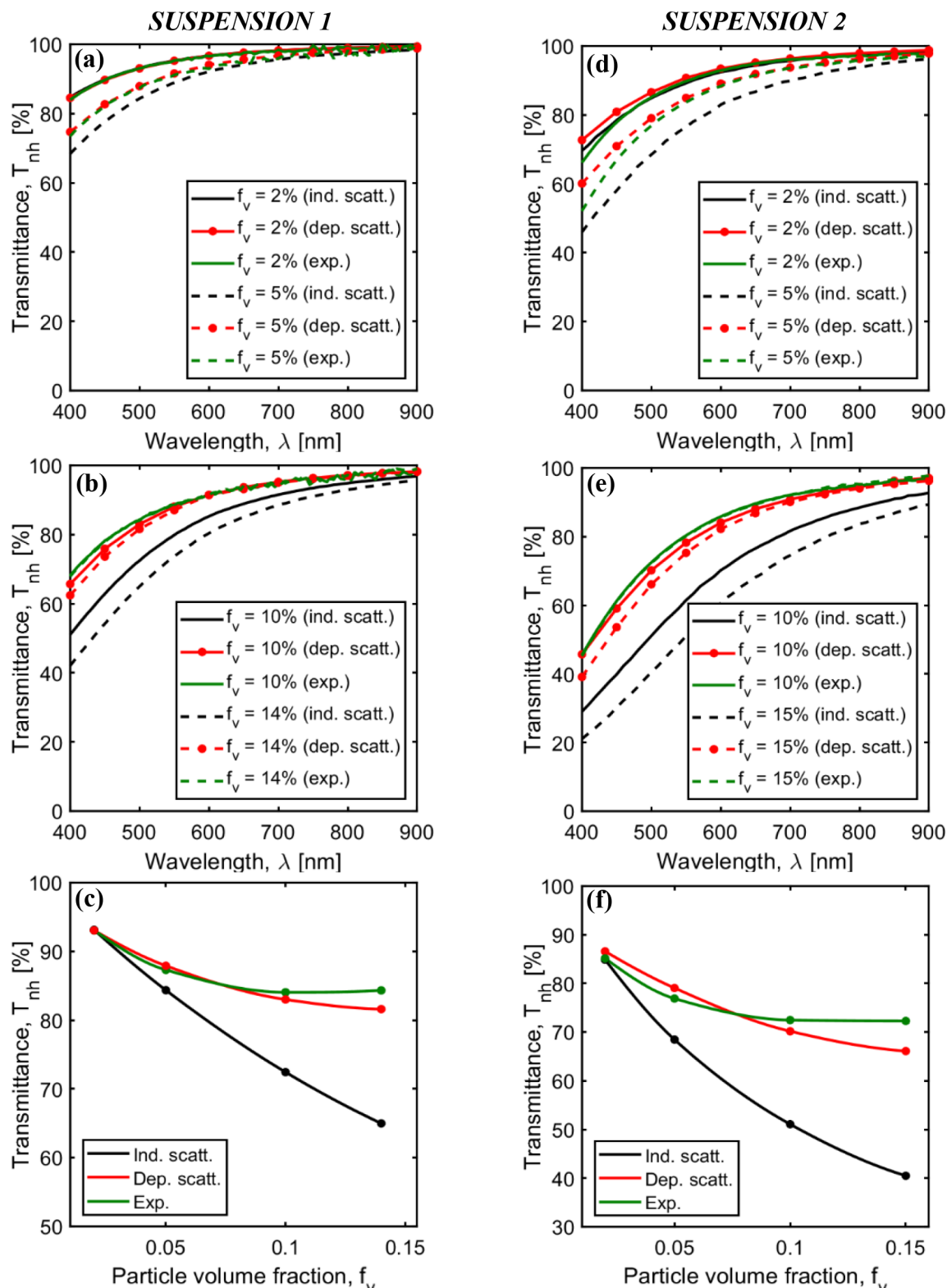


Figure 5. Comparison of the spectral transmittance $T_{nh,\lambda}$ measured experimentally and predicted by the R^2T^2 method accounting for dependent scattering and the classical Monte Carlo method assuming independent scattering for (a–c) Suspension 1 and (d–f) Suspension 2 and for (a, d) $f_v = 2\%$ or $f_v = 5\%$ and (b, e) $f_v = 10\%$ or $f_v = 14\%$ in the spectral window 400–900 nm. Normal-hemispherical transmittance $T_{nh,500}$ at 500 nm for (c) Suspension 1 and (f) Suspension 2 vs particle volume fraction f_v . In all cases, the colloidal suspension thickness was $L = 10$ mm.

R^2T^2 method. However, the predictions of the transmittance T_{nh} obtained by the DMRT method deviated from those obtained by solving Maxwell's equations for larger particles with radius $r_s = 150$ nm (Figure 4c), associated with stronger

light scattering. Second, excellent agreement was observed between predictions by the R^2T^2 method and by the T-matrix method for all particle size distribution and volume fraction f_v investigated. Indeed, predictions by the R^2T^2 method fell

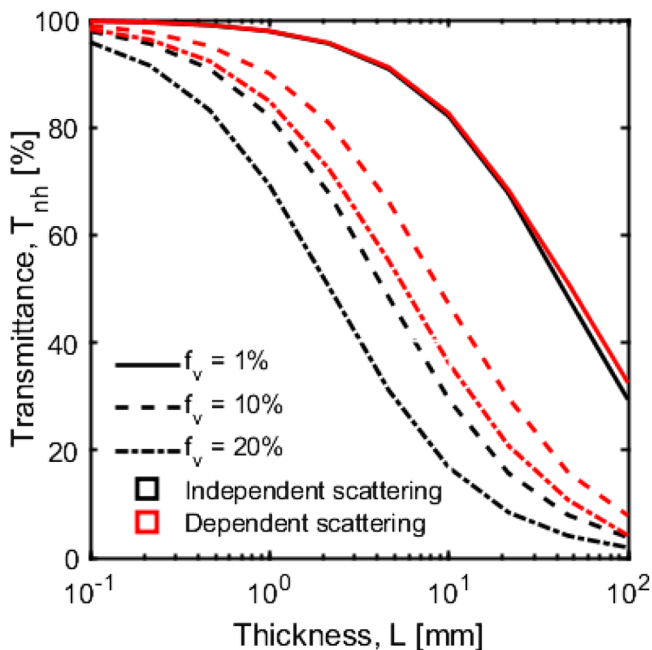


Figure 6. Predicted normal-hemispherical transmittance T_{nh} at $\lambda = 500$ nm for colloidal suspensions consisting of monodisperse nonabsorbing particles of radius $r_s = 10$ nm, relative refractive index $n = 1.5$, and volume fraction $f_v = 1\%$, 10% , or 20% as a function of suspension thickness L assuming independent scattering (classical Monte Carlo) and accounting for dependent scattering (R^2T^2 method).

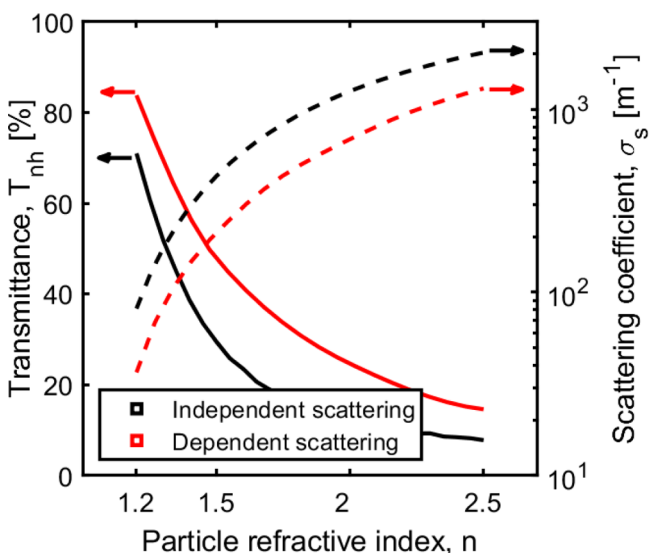


Figure 7. Normal-hemispherical transmittance T_{nh} and scattering coefficient σ_s at $\lambda = 500$ nm of a colloidal suspension of thickness $L = 10$ mm, consisting of monodisperse particles of radius $r_s = 10$ nm, volume fraction $f_v = 10\%$, as a function of their and relative particle refractive index n for $k = 0$ and by assuming either independent or dependent scattering.

within the uncertainty of the predictions from the T-matrix method used as a reference. These results demonstrated the validity and capabilities of the R^2T^2 method in accounting for dependent scattering as accurately as the T-matrix method while also being capable of simulating thick suspensions (Figure 4d). Note that a minor discrepancy was observed between the predictions by the R^2T^2 method and the T-matrix

method for large particle volume fraction and large particle radius, as illustrated in Figure 4c for monodisperse particles with $r_s = 150$ nm. This discrepancy can be attributed to specular reflections at the boundary of the computational domain, which were accounted for by the T-matrix method but not by the R^2T^2 method.

Moreover, predictions from solving the RTE assuming independent scattering agreed with predictions from the T-matrix and the R^2T^2 methods for relatively small volume fractions $f_v \leq 0.02$. This confirms that independent scattering prevailed for dilute colloidal suspensions. However, significant deviations were observed between the solution of the RTE assuming independent scattering and predictions by the T-matrix and R^2T^2 methods as the particle volume fraction f_v increased and as the particle radius r_s decreased. This can unequivocally be attributed to dependent scattering. It is interesting to note that dependent scattering resulted in a significantly larger normal-hemispherical transmittance T_{nh} than that obtained when assuming independent scattering. In other words, assuming independent scattering overestimated the scattering coefficient and the optical thickness of the suspension. Note also that for large particle volume fraction ($f_v \geq 0.1$) and small particles ($r_s \leq 50$ nm), the transmittance T_{nh} plateaued and even increased as the particle volume fraction f_v increased. These results are particularly surprising at first since the widely used independent scattering assumption indicates that the scattering coefficient increases with increasing particle volume fraction f_v and decreasing particle radius r_s , as is evident from eq 3.

5.2. Experiments. The objective of this section is to validate experimentally the R^2T^2 method using spectral normal-hemispherical transmittance measurements between 400 and 900 nm for the two types of previously described colloidal suspensions of silica nanoparticles in 10 mm thick quartz cuvettes with different dilution ratios and particle volume fractions. The spectral refractive index of silica and water in the spectral range of interest were taken from ref 55. Figure 5 compares predictions of the R^2T^2 method, accounting for particle polydispersity, with experimental measurements for the spectral normal-hemispherical transmittance $T_{nh,\lambda}$ of Suspension 1 featuring (a) $f_v = 2\%$ or 5% and (b) $f_v = 10\%$ or 14% and of Suspension 2 with (d) $f_v = 2\%$ or 5% and (e) $f_v = 10\%$ or 15% . Figure 5c,f also show the normal-hemispherical transmittance $T_{nh,500}$ at $\lambda = 500$ nm as a function of particle volume fraction f_v . In all plots, solutions of the RTE using the Monte Carlo method and assuming independent scattering are also shown. Given the experimental uncertainty in the measured volume fraction and particle size distribution and in the assumption that the particles are perfectly spherical, Figure 5 establishes that predictions of the R^2T^2 method agreed well with experimental measurements across the visible spectrum for both suspensions and all volume fractions considered. For both suspensions, assuming independent scattering led to reasonable predictions for particle volume fraction $f_v \leq 5\%$ when predictions by the R^2T^2 method and the classical Monte Carlo were comparable and in good agreement with experimental measurements. However, the effect of dependent scattering became more and more apparent with increasing volume fraction f_v . In fact, experimental measurements of $T_{nh,\lambda}$ feature a plateau and even a rise with increasing particle volume fraction f_v (see Figure 5c,f). By contrast, assuming independent scattering predicted a monotonously decreasing transmittance $T_{nh,\lambda}$ with volume fraction f_v resulting

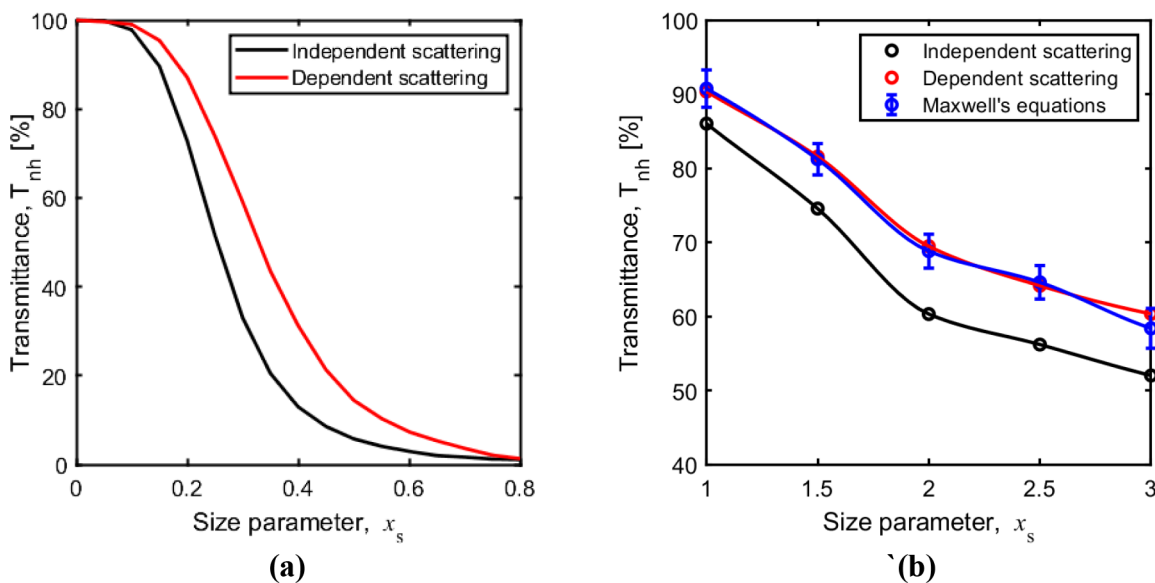


Figure 8. (a, b) Normal-hemispherical transmittance T_{nh} predicting assuming independent scattering or dependent scattering accounting only for the incoherent contribution or full solution of Maxwell's equations as functions of particle size parameter x_s with $r_s = 150 \text{ nm}$, $f_v = 20\%$, $m = n = 1.5$, for (a) $L = 2 \text{ mm}$ and (b) $L = 2 \mu\text{m}$.

in significant underestimation for $f_v > 5\%$. These results demonstrate the capability of the R^2T^2 method in predicting light transfer in nanoparticle suspensions when either independent or dependent scattering prevail.

5.3. Effect of Colloidal Suspension Thickness. Increasing the thickness of the colloidal suspension increases its optical thickness and the occurrence of multiple scattering. However, the thickness has no effect on dependent scattering since the ergodicity of the particle systems and the average interparticle distance is independent of thickness. Conveniently, predicting the transmittance T_{nh} using the R^2T^2 method for different thicknesses does not require reevaluation of Steps 1 and 2 corresponding to the generation of the N particle ensembles and the calculations of the incoherent T-matrix. In fact, only Step 3, consisting of solving the RTE using the Monte Carlo method must be performed for different thicknesses.

Figure 6 plots the normal-hemispherical transmittance T_{nh} at $\lambda = 500 \text{ nm}$ predicted as a function of suspension thickness L by solving the RTE accounting for dependent scattering (R^2T^2 method) or assuming independent scattering (classical Monte Carlo method) for colloidal suspensions with monodisperse silica particles of radius $r_s = 10 \text{ nm}$, relative refractive index $m = 1.5$, and volume fraction $f_v = 1\%$, 10% , and 20% . As expected, the transmittance T_{nh} decreased with increasing suspension thickness L for any given particle volume fraction f_v . Predictions of both solution methods agree with one another for volume fraction $f_v = 1\%$, as independent scattering prevailed. However, this was not the case for $f_v = 10\%$ and $f_v = 20\%$, when the R^2T^2 method predicted larger transmittance T_{nh} than the solution of the RTE assuming independent scattering. The discrepancy can be attributed to the prevalence of (i) dependent scattering for larger particle volume fraction f_v and (ii) multiple scattering for larger suspension thickness L . In fact, dependent scattering prevailed also in thick suspensions and manifested itself in the scattering coefficient and the scattering phase function which are independent of the suspension thickness. However, the transmittance is not only affected by the scattering coefficient

and the scattering phase function but also by the suspension thickness. As thickness increased, multiple scattering became significant and made the suspension opaque (i.e., $T_{nh} \rightarrow 0$).

5.4. Effect of Particle Refractive Index. Figure 7 plots the normal-hemispherical transmittance T_{nh} at $\lambda = 500 \text{ nm}$ and the associated average scattering coefficient σ_s considering either independent or dependent scattering for 10 mm thick suspensions consisting of monodisperse particles of radius $r_s = 10 \text{ nm}$, volume fraction $f_v = 10\%$, and relative refractive index n arbitrarily chosen such that (a) n ranged from 1.2 to 2.5 with $k = 0$. Figure 7 indicates that increasing the relative refractive index n of the particles enhanced the scattering coefficient σ_s and reduced the transmittance T_{nh} whether dependent scattering was considered or not. Nonetheless, for all values of n considered, assuming independent scattering resulted in a significant overestimation of the scattering coefficient σ_s and, thus, the underestimation of the transmittance compared to when dependent scattering was accounted for.

5.5. Effect of Particle Size Parameter x_s . Figure 4 indicated that the discrepancy in the normal-hemispherical transmittance T_{nh} between assuming independent scattering (classical Monte Carlo method) and accounting for dependent scattering (R^2T^2 method) decreased with increasing particle size. It also established that suspensions with polydisperse particles scattered light more than those with monodisperse particles for the same mean particle radius r_s and volume fraction f_v . In other words, dependent scattering was stronger for small and monodisperse particles than for larger and/or polydisperse particles. Consequently, this section inspects the effect of the particle size parameter x_s on the suspension's normal-hemispherical transmittance T_{nh} .

Figure 8 shows the normal-hemispherical transmittance T_{nh} of nonabsorbing colloidal suspensions predicted by solving the RTE either assuming independent scattering or considering dependent scattering as a function of the particle size parameter x_s for two different thicknesses, namely, (a) $L = 2 \text{ mm}$ and (b) $L = 2 \mu\text{m}$. Here, the particles were monodisperse with volume fraction $f_v = 20\%$ and relative refractive index $m = n = 1.5$. First, it is evident that for the range of size parameter

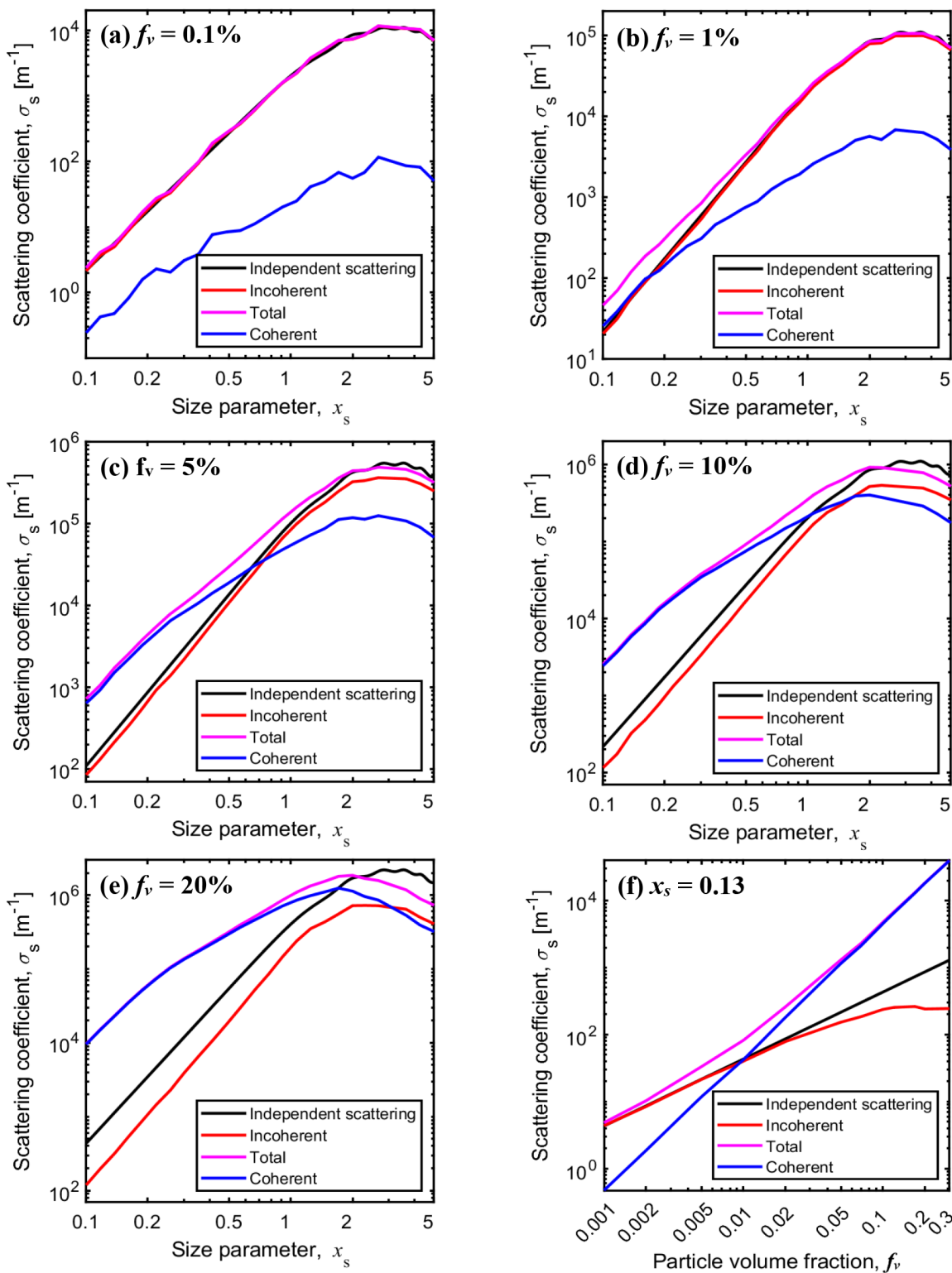


Figure 9. Total scattering coefficient σ_s^{ind} assuming independent scattering and ensemble-averaged coherent σ_s^c , incoherent σ_s^{ic} , and total (coherent + incoherent) $\sigma_s^c + \sigma_s^{ic}$ scattering coefficients predicted by the T-matrix method as functions of particle size parameter x_s for different particle volume fractions f_v . Scattering coefficients and components of colloidal suspensions consisting of monodisperse particles and particle relative refractive index $n = 1.5$ at $\lambda = 500$ nm as a function of (a–e) x_s and (f) f_v by assuming either independent or dependent scattering.

x_s and for both thicknesses considered, large discrepancies existed between the two approaches, indicating that dependent scattering prevailed. This was confirmed by the good agreement obtained between predictions of the R²T² method and those obtained by solving Maxwell's equations using the

superposition T-matrix method for the thinnest slab of thickness $L = 2 \mu\text{m}$ (Figure 8b).

According to the scattering regime map proposed by Tien and Drolen³⁵ and previously reviewed, dependent scattering is expected to vanish for $f_v = 20\%$ and $x_s \geq 2.87$ (eq 5). However,

Figure 8 indicates that dependent scattering was still significant for $f_v = 20\%$ and $x_s = 3$. Our results were consistent with those reported by Mishchenko et al.²⁰ who experimentally observed dependent scattering in a latex nanoparticle suspended in water with $f_v = 10\%$, $L = 2$ mm, $x_s = 4.2$, and $x = 4.9$. For $f_v = 10\%$, the above criterion indicates that independent scattering should prevail for $x_s > 1.65$, in contradiction with experimental observations. Discrepancies between the above criterion, used by numerous studies, and the present approach adopted from rigorous treatments of electromagnetic scattering lie in the fact that the latter deal with the incoherent scattering coefficient σ_s^{ic} instead of the total scattering coefficient σ_s .

Figure 9 compares the average (i) coherent σ_s^c , (ii) incoherent σ_s^{ic} , and (iii) total (coherent + incoherent) $\sigma_s^c + \sigma_s^{ic}$ scattering coefficients of suspensions of monodisperse nonabsorbing nanoparticles in vacuum ($n = 1.5$), predicted by the superposition T-matrix method for N particle ensembles, as functions of particle size parameter x_s for particle volume fraction f_v between 0.1% and 20%. As a reference, it also plots the total scattering coefficient σ_s^{ind} assuming independent scattering (eq 3). It is important to note that scattering by a sphere (Lorenz-Mie theory) or by an ensemble of particles (superposition T-matrix method) were performed assuming that the surrounding medium was vacuum, that is, $n_m = 1.0$. However, the scattering characteristics obtained by simulating the electromagnetic scattering using the superposition T-matrix method by an ensemble of spheres in free space does not represent the scattering characteristics of the colloidal suspension alone. Indeed, the incident EM wave gets scattered not only by the nanoparticles randomly distributed in the computational domain but also by the domain boundaries. The contribution of the domain boundaries to scattering is accounted for the coherent scattering coefficient σ_s^c , whereas the incoherent scattering coefficient σ_s^{ic} accounts for the scattering by the dispersed particles contained within the domain.²³ Figure 9 indicates that for dilute suspensions (e.g., $f_v = 0.1\%$), the coherent scattering coefficient σ_s^c was negligible compared with the incoherent scattering coefficient σ_s^{ic} . This can be explained by the fact that the mismatch in the effective refractive index between the computational domain and the surrounding is very small. In addition, for $f_v = 0.1\%$, it is evident that $\sigma_s^{ic} = \sigma_s^{ind}$ for all size parameter x_s considered (Figure 9a). This establishes that independent scattering prevailed and that the incoherent contribution σ_s^{ic} to the total scattering coefficient for a particle ensemble captures solely the scattering by the dispersed particles. Similar observations could be made for $f_v = 1\%$ when independent scattering prevailed (Figure 9b). However, for small values of x_s , the coherent scattering coefficient σ_s^c due to boundary scattering was significant thus establishing that σ_s^c needs to be dissociated from σ_s^{ic} . As the volume fraction increased beyond $f_v \geq 5\%$ (Figures 9c–e), σ_s^{ic} followed the same trends as σ_s^{ind} but was systematically smaller for all size parameters considered. This discrepancies between σ_s^{ic} and σ_s^{ind} increased with increasing volume fraction f_v . These observations can be attributed to dependent scattering. Here also, the coherent scattering coefficient σ_s^c was significant for small values of x_s .

6. CONCLUSION

This study demonstrates numerically and experimentally that dependent scattering occurs in concentrated nonabsorbing colloidal suspensions with particle volume fraction as low as 1–2%. First, we developed a new numerical framework

simulating radiation transfer in dense nonabsorbing colloidal suspensions of arbitrary thickness accounting for dependent scattering and multiple scattering based on the Radiative Transfer with Reciprocal Transactions (R^2T^2) method. The numerical predictions were validated by showing excellent agreement with the spectral normal-hemispherical transmittance in the visible part of the electromagnetic spectrum (i) predicted by the superposition T-matrix method for thin suspensions and (ii) measured experimentally on colloidal suspensions of silica nanoparticles with particle diameter between 16 and 28 nm and volume fraction up to 15%. Dependent scattering effects, captured by the incoherent scattering coefficient, become significant with decreasing particle size and increasing volume fraction and index mismatch between the particles and their surroundings. Interestingly, dependent scattering effects can cause the transmittance of colloidal suspensions to increase with increasing particle volume fraction. However, assuming independent scattering resulted in major overestimation of the scattering coefficient and underestimation of transmittance of concentrated colloidal suspensions. Finally, this experimentally-validated method can be used to simulate light transfer in dense and thick suspensions of nonspherical and/or absorbing particles, randomly distributed, ordered, or aggregated.

AUTHOR INFORMATION

Corresponding Author

Laurent Pilon – Mechanical and Aerospace Engineering Department, University of California, Los Angeles, Los Angeles, California 90095-1597, United States; California NanoSystems Institute and Institute of the Environment and Sustainability, University of California, Los Angeles, Los Angeles, California 90095, United States;  orcid.org/0000-0001-9459-8207; Email: pilon@seas.ucla.edu

Authors

Refet Ali Yalcin – Mechanical and Aerospace Engineering Department, University of California, Los Angeles, Los Angeles, California 90095-1597, United States;  orcid.org/0000-0003-3997-3494

Thomas Lee – Mechanical and Aerospace Engineering Department, University of California, Los Angeles, Los Angeles, California 90095-1597, United States

Ghareh Natalie Kashanchi – Chemistry Department, University of California, Los Angeles, Los Angeles, California 90095-1597, United States

Johannes Markkanen – Institut für Geophysik und Extraterrestrische Physik, Technische Universität Braunschweig, 38106 Braunschweig, Germany; Max Planck Institute for Solar System Research, Göttingen 37077, Germany;  orcid.org/0000-0001-5989-3630

Ricardo Martinez – Mechanical and Aerospace Engineering Department, University of California, Los Angeles, Los Angeles, California 90095-1597, United States

Sarah H. Tolbert – Chemistry Department, University of California, Los Angeles, Los Angeles, California 90095-1597, United States; California NanoSystems Institute, University of California, Los Angeles, Los Angeles, California 90095, United States;  orcid.org/0000-0001-9969-1582

Complete contact information is available at:

<https://pubs.acs.org/10.1021/acsphtronics.2c00664>

Funding

This research was also supported in part by Advanced Research Projects Agency-Energy (ARPA-E) Single-Pane Highly Insulating Efficient Lucid Designs (SHIELD) Program (ARPA-E Award DE-AR0000738). R.A.Y. is grateful for financial support from the Fulbright Scholar Program (FY-2020-TR-PD-12).

Notes

The authors declare no competing financial interest.

ACKNOWLEDGMENTS

This work used computational and storage services associated with the Hoffman2 Shared Cluster provided by UCLA Institute for Digital Research and Education's Research Technology Group.

NOMENCLATURE

a_{vv1} , a_{vv2}	outgoing electric field coefficients (eq 8)
C_{abs}	absorption cross-section (nm^2)
C_{sca}	scattering cross-section (nm^2)
E^{sca}	scattered electromagnetic field (V m^{-1})
$E^{sca,c}$	scattered coherent electromagnetic field (V m^{-1})
$E^{sca,ic}$	scattered incoherent electromagnetic field (V m^{-1})
f_v	particle volume fraction
I_λ	spectral radiation intensity ($\text{W m}^{-2} \text{ sr}^{-1} \text{ nm}^{-1}$)
k_s	particle absorption index
L	colloidal suspension thickness (mm)
N	number of particle ensembles
N_c	number of particles in an ensemble
m_s	particle complex index of refraction, $m_s = n_s + ik_s$
m	particle relative complex index of refraction, $m = m_s/n_m$
n_s	particle refractive index
n_m	continuous medium refractive index
N_T	number of particles per unit volume of suspension (m^{-3})
n	particle relative refractive index, $n = n_s/n_m$
q	angular wavenumber, $q = 2\pi/\lambda$ (m^{-1})
R_c	radius of cylinder filled with particles (m)
r_s	particle radius (nm)
T	Total T-matrix, $T = T^{ic} + T^c$
T^{ic}	incoherent T-matrix
T^c	coherent T-matrix
V_e	volume of particle ensemble (nm^3)
x_s	particle size parameter, $x_s = 2\pi r_s/\lambda$
x	silica particle mass fraction in suspension

Greek Symbols

β	extinction coefficient (m^{-1})
κ	absorption coefficient (m^{-1})
λ	wavelength in vacuum (nm)
ρ	density (g/cm^3)
σ	particle radius standard deviation (nm)
σ_s	scattering coefficient (m^{-1})
Φ_T	suspension scattering phase function
ω	single scattering albedo
Ω	solid angle (sr)

Subscripts

λ	refers to spectral value
i	refers to the i^{th} particle ensemble ($1 \leq i \leq N$)
s	refers to silica particles
w	refers to water

Superscripts

c	refers to coherent radiation
ic	refers to incoherent radiation

REFERENCES

- Orel, B.; Gunde, M. K.; Krainer, A. Radiative cooling efficiency of white pigmented paints. *Sol. Energy* **1993**, *50*, 477–82.
- Uemoto, K. L.; Sato, N. M. N.; John, V. M. Estimating thermal performance of cool colored paints. *Energy and Buildings* **2010**, *42*, 17–22.
- Tesfamichael, T.; Hoel, A.; Wäckelgård, E.; Niklasson, G. A.; Gunde, M. K.; Orel, Z. C. Optical characterization and modeling of black pigments used in thickness-sensitive solar-selective absorbing paints. *Sol. Energy* **2001**, *69*, 35–43.
- Otanicar, T. P.; Phelan, P. E.; Prasher, R. S.; Rosengarten, G.; Taylor, R. A. Nanofluid-based direct absorption solar collector. *Journal of Renewable and Sustainable Energy* **2010**, *2*, 033102.
- Saidur, R.; Meng, T. C.; Said, Z.; Hasanuzzaman, M.; Kamyar, A. Evaluation of the effect of nanofluid-based absorbers on direct solar collector. *Int. J. Heat Mass Transfer* **2012**, *55*, 5899–907.
- Tyagi, H.; Phelan, P.; Prasher, R. Predicted Efficiency of a Low-Temperature Nanofluid-Based Direct Absorption Solar Collector. *Journal of Solar Energy Engineering* **2009**, *131*.
- Miller, F. J.; Koenigsdorff, R. W. Thermal Modeling of a Small-Particle Solar Central Receiver. *Journal of Solar Energy Engineering* **2000**, *122*, 23–9.
- Abdelrahman, M.; Fumeaux, P.; Suter, P. Study of solid-gas-susensions used for direct absorption of concentrated solar radiation. *Sol. Energy* **1979**, *22*, 45–8.
- Mishchenko, M. I.; Cairns, B.; Hansen, J. E.; Travis, L. D.; Burg, R.; Kaufman, Y. J.; et al. Monitoring of aerosol forcing of climate from space: analysis of measurement requirements. *Journal of Quantitative Spectroscopy and Radiative Transfer* **2004**, *88*, 149–61.
- Plass, G. N.; Kattawar, G. W. Monte Carlo Calculations of Light Scattering from Clouds. *Appl. Opt.* **1968**, *7*, 415.
- Zhu, J.; Chen, Y.; Zhang, L.; Jia, X.; Feng, Z.; Wu, G.; et al. Demonstration of measuring sea fog with an SNSPD-based Lidar system. *Sci. Rep.* **2017**, *7*, 15113.
- Mishchenko, M. I. Asymmetry parameters of the phase function for densely packed scattering grains. *Journal of Quantitative Spectroscopy and Radiative Transfer* **1994**, *52*, 95–110.
- Kim, H. S.; Mason, T. G. Advances and challenges in the rheology of concentrated emulsions and nanoemulsions. *Adv. Colloid Interface Sci.* **2017**, *247*, 397–412.
- Schramm, L. L. Front Matter. *Emulsions, Foams, and Suspensions: Fundamentals and Applications*; Wiley-VCH Verlag GmbH & Co. KGaA, 2006; pp I–XV. DOI: [10.1002/3527606750.fmatter](https://doi.org/10.1002/3527606750.fmatter).
- Tadros, T. F. Front Matter. *Applied Surfactants*; Wiley-VCH Verlag GmbH & Co. KGaA, 2005; pp i–xx. DOI: [10.1002/3527604812.fmatter](https://doi.org/10.1002/3527604812.fmatter).
- Mason, T. G.; Wilking, J. N.; Meleson, K.; Chang, C. B.; Graves, S. M. Nanoemulsions: formation, structure, and physical properties. *J. Phys.: Condens. Matter* **2006**, *18*, R635.
- Modest, M. F. *Radiative Heat Transfer*; Academic Press, 2013. DOI: [10.1016/C2010-0-65874-3](https://doi.org/10.1016/C2010-0-65874-3).
- Galy, T.; Huang, D.; Pilon, L. Revisiting independent versus dependent scattering regimes in suspensions or aggregates of spherical particles. *Journal of Quantitative Spectroscopy and Radiative Transfer* **2020**, *246*, 106924.
- Mishchenko, M. I. Independent" and "dependent" scattering by particles in a multi-particle group. *OSA Continuum* **2018**, *1*, 243.
- Markkanen, J.; Väistönen, T.; Penttilä, A.; Muinonen, K. Scattering and absorption in dense discrete random media of irregular particles. *Opt. Lett.* **2018**, *43*, 2925.
- Nguyen, V. D.; Faber, D. J.; van der Pol, E.; van Leeuwen, T. G.; Kalkman, J. Dependent and multiple scattering in transmission and backscattering optical coherence tomography. *Opt. Express* **2013**, *21*, 29145.
- Fujii, H.; Tsang, L.; Zhu, J.; Nomura, K.; Kobayashi, K.; Watanabe, M. Photon transport model for dense polydisperse colloidal suspensions using the radiative transfer equation combined with the dependent scattering theory. *Opt. Express* **2020**, *28*, 22962.

- (23) Muinonen, K.; Markkanen, J.; Väisänen, T.; Peltoniemi, J.; Penttilä, A. Multiple scattering of light in discrete random media using incoherent interactions. *Opt. Lett.* **2018**, *43*, 683.
- (24) Väisänen, T.; Markkanen, J.; Penttilä, A.; Muinonen, K. Radiative transfer with reciprocal transactions: Numerical method and its implementation. *PLoS One* **2019**, *14*, No. e0210155.
- (25) Markkanen, J.; Yuffa, A. J. Fast superposition T-matrix solution for clusters with arbitrarily-shaped constituent particles. *Journal of Quantitative Spectroscopy and Radiative Transfer* **2017**, *189*, 181–8.
- (26) Galy, T.; Pilon, L. Dependent scattering effects in aggregates with touching or overlapping non-absorbing spherical particles. *Journal of Quantitative Spectroscopy and Radiative Transfer* **2022**, *278*, 108018.
- (27) Yee, K. S.; Chen, J. S. The finite-difference time-domain (FDTD) and the finite-volume time-domain (FVTD) methods in solving Maxwell's equations. *IEEE Transactions on Antennas and Propagation* **1997**, *45*, 354–63.
- (28) Draine, B. T.; Flatau, P. J. Discrete-Dipole Approximation For Scattering Calculations. *Journal of the Optical Society of America A* **1994**, *11*, 1491.
- (29) Monk, P. *Finite Element Methods for Maxwell's Equations*; Oxford University Press, 2003. DOI: [10.1093/acprof:oso/9780198508885.001.0001](https://doi.org/10.1093/acprof:oso/9780198508885.001.0001).
- (30) Mackowski, D. W.; Mishchenko, M. I. A multiple sphere T-matrix Fortran code for use on parallel computer clusters. *Journal of Quantitative Spectroscopy and Radiative Transfer* **2011**, *112*, 2182–92.
- (31) Penttilä, A.; Markkanen, J.; Väisänen, T.; Räbinä, J.; Yurkin, M. A.; Muinonen, K. How much is enough? The convergence of finite sample scattering properties to those of infinite media. *Journal of Quantitative Spectroscopy and Radiative Transfer* **2021**, *262*, 107524.
- (32) Baran, A. J.; Yang, P.; Havemann, S. Calculation of the single-scattering properties of randomly oriented hexagonal ice columns: a comparison of the T-matrix and the finite-difference time-domain methods. *Appl. Opt.* **2001**, *40*, 4376.
- (33) Mie, G. Beiträge zur Optik trüber Medien, speziell kolloidaler Metallösungen. *Ann. Phys.* **1908**, *330*, 377–445.
- (34) Egel, A.; Pattelli, L.; Mazzamuto, G.; Wiersma, D. S.; Lemmer, U. CELES: CUDA-accelerated simulation of electromagnetic scattering by large ensembles of spheres. *Journal of Quantitative Spectroscopy and Radiative Transfer* **2017**, *199*, 103–10.
- (35) Tien, C. L.; Drolen, B. L. Thermal radiation in particulate media with dependent and independent scattering. *Annual Review of Numerical Fluid Mechanics and Heat Transfer*; Hemisphere Publishing Corp., 1987; Vol. 1, pp 1–32.
- (36) Brewster, M. Q.; Tien, C. L. Radiative Transfer in Packed Fluidized Beds: Dependent Versus Independent Scattering. *Journal of Heat Transfer* **1982**, *104*, 573–9.
- (37) Cartigny, J. D.; Yamada, Y.; Tien, C. L. Radiative Transfer With Dependent Scattering by Particles: Part 1—Theoretical Investigation. *Journal of Heat Transfer* **1986**, *108*, 608–13.
- (38) Yamada, Y.; Cartigny, J. D.; Tien, C. L. Radiative Transfer With Dependent Scattering by Particles: Part 2—Experimental Investigation. *Journal of Heat Transfer* **1986**, *108*, 614–8.
- (39) Drolen, B. L.; Tien, C. L. Independent and dependent scattering in packed-sphere systems. *Journal of Thermophysics and Heat Transfer* **1987**, *1*, 63–8.
- (40) Galy, T.; Pilon, L. Dependent scattering effects in aggregates with touching or overlapping non-absorbing spherical particles. *Journal of Quantitative Spectroscopy and Radiative Transfer* **2021**, *108018*.
- (41) Mishchenko, M. I. Multiple scattering by particles embedded in an absorbing medium. 1. Foldy-Lax equations, order-of-scattering expansion, and coherent field. *Opt. Express* **2008**, *16*, 2288.
- (42) Fujii, H.; Ueno, M.; Inoue, Y.; Aoki, T.; Kobayashi, K.; Watanabe, M. Model equations of light scattering properties and a characteristic time of light propagation for polydisperse colloidal suspensions at different volume fractions. *Opt. Express* **2022**, *30*, 3538.
- (43) Tsang, L.; Ishimaru, A. Radiative Wave Equations for Vector Electromagnetic Propagation in Dense Nontenuous Media. *Journal of Electromagnetic Waves and Applications* **1987**, *1*, 59–72.
- (44) Tsang, L.; Kong, J. A.; Ding, K.-H.; Ao, C. O. Dense Media Models and Three-Dimensional Simulations. *Scattering of Electromagnetic Waves: Numerical Simulations*; John Wiley & Sons, Inc.: New York, U.S.A., 2002; pp 495–549. DOI: [10.1002/0471224308.ch10](https://doi.org/10.1002/0471224308.ch10).
- (45) Zurk, L. M.; Tsang, L.; Winebrenner, D. P. Scattering properties of dense media from Monte Carlo simulations with application to active remote sensing of snow. *Radio Science* **1996**, *31*, 803–19.
- (46) Waterman, P. C. Matrix formulation of electromagnetic scattering. *Proceedings of the IEEE* **1965**, *53*, 805–12.
- (47) Laaksonen, K.; Li, S. Y.; Puisto, S. R.; Rostedt, N. K. J.; Alaniissila, T.; Granqvist, C. G.; et al. Nanoparticles of TiO₂ and VO₂ in dielectric media: Conditions for low optical scattering, and comparison between effective medium and four-flux theories. *Sol. Energy Mater. Sol. Cells* **2014**, *130*, 132–7.
- (48) Elaloufi, R.; Carminati, R.; Greffet, J.-J. Definition of the diffusion coefficient in scattering and absorbing media. *Journal of the Optical Society of America A* **2003**, *20*, 678.
- (49) Hassan, P. A.; Rana, S.; Verma, G. Making Sense of Brownian Motion: Colloid Characterization by Dynamic Light Scattering. *Langmuir* **2015**, *31*, 3–12.
- (50) Yalcin, R. A. Solution of RTE with Monte Carlo method and Mie theory. <https://github.com/refetaliyalcin/monte-carlo-mie-scattering> (accessed 2022–02–13).
- (51) Yalcin, R. A. Solution of RTE with Monte Carlo method and Mie theory for polydispersed spheres. <https://github.com/refetaliyalcin/monte-carlo-mie-scattering-polydisperse-particles> (accessed 2022–02–13).
- (52) Yalcin, R. A.; Blandre, E.; Joulain, K.; Drévillon, J. Colored Radiative Cooling Coatings with Nanoparticles. *ACS Photonics* **2020**, *7*, 1312–22.
- (53) Incoherent volume element generator (IVEGen). https://bitbucket.org/planetarysystemresearch/ivegen_pub (accessed 2022–09–10).
- (54) Rumble, J. *CRC Handbook of Chemistry and Physics*, 98th ed.; CRC Press: London, 2017.
- (55) Kitamura, R.; Pilon, L.; Jonasz, M. Optical constants of silica glass from extreme ultraviolet to far infrared at near room temperature. *Appl. Opt.* **2007**, *46*, 8118.